Numerical Simulation of Wavelength-Dependent Laser-Induced Breakdown for Improved Laser Applications

VIOLETA PETROVIĆ[1], HRISTINA DELIBAŠIĆ MARKOVIĆ[1], IVAN PETROVIĆ[2]
[1]Faculty of Science,
University of Kragujevac,
Radoja Domanovića 12, 34000 Kragujevac,
SERBIA

[2]Department in Kragujevac,
Academy of Professional Studies Šumadija,
Kosovska 8, 34000 Kragujevac,
SERBIA

Abstract: - Laser-induced breakdown plays a crucial role in laser applications. Consequently, investigating the influence of different parameters is important for improving and optimizing laser-based applications. This work examines the wavelength dependence of breakdown in air using a model that couples a free-electron rate equation with a two-temperature plasma description. The model includes multiphoton and avalanche ionization as the main electron generation processes, as well as recombination, attachment, diffusion, and inverse bremsstrahlung absorption, which are responsible for electron losses from the volume. Numerical results are obtained for two representative wavelengths, $\lambda = 355\,nm$ and $\lambda = 532nm$, under comparable pulse and focusing conditions. We show that plasma formation at shorter wavelengths is more efficiently initiated through multiphoton ionization, whereas at higher wavelengths, stronger inverse bremsstrahlung heating enhances avalanche ionization, resulting in higher electron densities and more pronounced plasma development.

Key-Words: - laser-matter interaction**,** laser-induced breakdown, two-temperature model, free-electron density, plasma formation, wavelength dependence, ultrashort laser pulses.

Received: October 7, 2025. Revised: April 17, 2026. Accepted: May 13, 2026. Published: August 6, 2026.

1 Introduction

Since the invention of high-power pulsed lasers, the phenomena of laser-induced breakdown (LIB) and damage to various materials have been extensively investigated [1], [2]. With the increasing development and application of lasers, numerous experimental techniques have been introduced to study the various processes responsible for LIB in different materials [3], [4]. These developments have allowed more precise and systematic investigations, while also revealing the complexity of the interconnected ionization mechanisms involved in LIB. During LIB, a rapid increase in temperature and pressure can cause various types of damage, including melting, vaporization, surface ablation, and the formation of microcracks. These damages may limit the laser application, and that is why, in biomedical and industrial laser applications, controlling the LIB threshold is essential to avoid them. On the other hand, LIB is intentionally utilized in applications such as laser ablation, micromachining, laser-induced breakdown spectroscopy (LIBS), and medical procedures where precise and localized laser–material interaction is required.

The first theoretical predictions, confirmed by numerical [5] and experimental [6] findings, have shown that when a short laser pulse interacts with a gas, electrons can be generated through multiphoton ionization (MPI) and electron-impact ionization (EII) events. Multiphoton ionization (MPI) is the initial process that generates the first photoelectrons. Subsequently, during electron-impact ionization (EII) events, electrons absorb energy from the laser field through inverse bremsstrahlung (IB) collisions with neutral particles, which consequently increases the electron density. Conversely, electrons may also lose energy through elastic and inelastic collisions with neutrals. Some electrons are additionally lost through diffusion or recombination processes. If the laser intensity is sufficiently high, a fraction of the residual electrons, despite these energy-loss mechanisms, can acquire energies exceeding the ionization potential. At sufficiently high fields, ionizing collisions will cause an electron avalanche ionization (AI) to occur, while leading to an exponential growth of the number of electrons. It is also worth noting that MPI can dominate AI only at short wavelengths or low densities. According to [7], this is because the ionization potential of most gases is relatively high, while the probability of simultaneous absorption quickly decreases with the number of photons required for ionization. As a result, the relative contribution of MPI and CI strongly depends on both the laser wavelength and the local plasma conditions.

Despite the long-standing recognition of the important role of LIB and related phenomena, much remains to be learned about the interaction of ultrashort laser pulses with a gas target. Research conducted in [8] and [9] introduced new approaches to laser damage studies, which opened opportunities for the development of novel laser systems and optical materials. Anyway, this period marked a transition from phenomenological observations toward more controlled and application-driven studies. [10] assumed that the plasma produced in the air goes through several stages of morphological development. Their two-dimensional temperature model, based on the fact that electron heating occurs on a much shorter timescale than energy transfer to the neutral gas, leads to two essential conclusions: first that the reverse pressure gradient propagates radially inwards and compresses the plasma in air, while forming a localized high-pressure zone at the center that generates a secondary pressure wave and second that the baroclinic torque that is generated because of the Richtmyer-Meshkov instability dominates the rate of vorticity. These results demonstrate that energy deposition during LIB rapidly translates into complex fluid-like behavior of plasma. Findings presented in [10] can be utilized for the control and optimization of laser-induced plasma (LIP) applications. Such insights are particularly relevant for tailoring breakdown conditions in practical systems.

Although considerable advances have been achieved in experimental and numerical investigations, a comprehensive model that consistently describes wavelength-dependent ionization processes in gaseous media is still lacking.

In this paper, we numerically solve a rate equation describing the evolution of the free-electron density and electron temperature generated by intense laser pulses in air. The electron rate equation accounts for the dominant gain and loss mechanisms relevant for LIB, while allowing for a wide range of laser intensities and wavelengths. The model is defined by key laser parameters such as pulse duration, wavelength, energy, and focusing conditions. Its main innovation is the consistent coupling of wavelength-dependent ionization processes with inverse bremsstrahlung absorption and two-temperature plasma dynamics in a single unified framework. In this approach, electrons and heavy particles are treated as separate subsystems, and their temperatures are calculated simultaneously by solving coupled energy equations using a finite-difference method. The model consistently links electron production, laser energy absorption, and energy exchange through collisions, which makes it possible to study how breakdown dynamics depend on wavelength. This allows a detailed investigation of electron density evolution, temperature nonequilibrium, and plasma channel formation under comparable laser conditions.

The structure of the paper is as follows. Section 2 presents the theoretical framework of the model, including the governing equations for electron density evolution, laser propagation, and the two-temperature energy balance. In Section 3, the numerical results are analyzed, with particular emphasis on the influence of laser parameters, especially the wavelength, on the breakdown dynamics. The main conclusions of the study are summarized in Section 4.

2 Theoretical framework

The theoretical framework governs the axial direction of laser propagation, where the strongest coupling between laser attenuation and plasma formation takes place, providing a physically intuitive and reasonably thorough account of breakdown dynamics and their relationship to laser wavelength. The model describes the early stages of LIB, clarifying the conditions that lead to subsequent strong hydrodynamic expansion and shock-wave formation, and consequently to LIB applications. The model uses the continuity equation, which accounts for the balance between generation and loss processes and is additionally supplemented by electron diffusion along the propagation axis, as follows, [11]:

$$\frac{\partial n_e(x,t)}{\partial t} = S_{MPI} + S_{av} - L_{rec} - L_{att} + \frac{\partial}{\partial x}\left(D_e \frac{\partial n_e}{\partial x}\right). \quad (1)$$

Here, the temporal and spatial dependence of free-electron density is assumed, $n_e(x,t) \equiv n_e$. The first two terms on the right side of Eq. 1, S_{MPI} and

S_{av}, represent MPI and AI contributions, respectively. The next two terms quantitatively describe the dominant electron loss processes: recombination and diffusion.

Equation 1 can be rewritten by considering the specific expressions for each of the aforementioned processes, [12]:

$$\frac{\partial n_e(x,t)}{\partial t} = \sigma_K I^K n_n + I n_e/(E_I(1 + \omega^2\tau_m^2)) - \beta_{\text{rec}} n_e^2 - k_{\text{att}} n_e n_{O_2} n_n + \frac{\partial}{\partial x}\left(D_e \frac{\partial n_e}{\partial x}\right). \quad (2)$$

Here σ_K is the effective $K -$ photon ionization coefficient, $I(x,t)$ the local laser intensity, K the minimum number of photons required to overcome the ionization potential, n_n the neutral particle density, E_I the effective ionization potential (it is assumed to be $E_I \approx 12.1$ eV), $\omega = 2\pi c/\lambda$ the laser angular frequency, λ laser wavelength, while τ_m denotes the effective electron momentum relaxation time typically in the femtosecond range for weakly ionized gases. In the recombination term (modelled as $L_{\text{rec}} = \beta_{\text{rec}} n_e^2$) β_{rec} is the effective recombination coefficient, taken as $\beta_{\text{rec}} \approx 2 \times 10^{-13}\ \text{m}^3\ \text{s}^{-1}$. In addition, three-body attachment to oxygen molecules is included via $L_{\text{att}} = k_{\text{att}} n_e n_{O_2} n_n$, where $n_{O_2} \approx 0.21\, n_n$ represents the oxygen fraction in air and $k_{\text{att}} \approx 10^{-43}\ \text{m}^6\ \text{s}^{-1}$ is the attachment rate coefficient. For the sake of calculation, for ambient air at atmospheric pressure and temperature $T_0 = 300$ K, the initial neutral electron density is taken as $n_n = p_0/(k_B T_0)$, with $p_0 = 101325$ Pa. All coefficients correspond to standard values reported for atmospheric-pressure air plasmas under weakly ionized conditions, [13], [14], [15].

Spatial transport of electrons is incorporated through the diffusion term. The diffusion coefficient is expressed as $D_e = k_B T_e/(m_e \nu_{en})$, where T_e is the electron temperature, m_e is the electron mass, and $\nu_{en} = n_n \sigma_{en} v_{th}$ is the electron-neutral collision frequency, with $\sigma_{en} \approx 2 \times 10^{-20}\ \text{m}^2$ and v_{th} the mean electron thermal velocity, $v_{th} = \sqrt{8 k_B T_e/\pi m_e}$, [13]. The initial background electron density is taken as $n_e(t = 0) \approx 10^8\ \text{m}^{-3}$, ensuring a physically realistic seed level for breakdown initiation, [12]. The relative contribution of MPI and AI is governed by the competition between the corresponding source terms, whose characteristic growth rates depend strongly on the laser wavelength. This formulation ensures that both local plasma growth and spatial spreading of the ionized region are consistently captured within the same framework.

The relative contributions of MPI and AI are determined by the relation between their corresponding source terms, whose characteristic growth rates are strongly dependent on the laser wavelength. This approach consistently describes both the local development of the plasma and the spatial expansion of the ionized region within a single unified framework.

The growth of the electron density is closely linked to the spatial evolution of the laser field. As the beam propagates through the medium, its intensity is progressively reduced due to collisional absorption in the partially ionized gas. This coupling between electron dynamics and energy deposition is described by the attenuation equation, [11]:

$$\frac{\partial I}{\partial x} = -\alpha_{\text{IB}}(n_e, T_e, \lambda)\, I, \quad (3)$$

where α_{IB} denotes the IB absorption coefficient. In the considered regime, this mechanism provides the dominant pathway for transferring energy from the laser field to free electrons. A commonly used expression for the absorption coefficient can be written in the form:

$$\alpha_{\text{IB}} \propto \frac{\omega_p^2}{c}\ \frac{\nu_{en}}{\omega^2 + \nu_{en}^2}, \quad (4)$$

where $\omega_p^2 = n_e e^2/(\varepsilon_0 m_e)$ is the plasma frequency and ν_{en} is the electron-neutral collision frequency. Under atmospheric conditions, typical electron-neutral collision frequencies lie in the range $\nu_{en} \sim 10^{12}$–$10^{13}\ \text{s}^{-1}$, depending on the electron temperature. For electron densities relevant to the onset of LIB, $n_e \sim 10^{20}$–$10^{23}\ \text{m}^{-3}$, the corresponding plasma frequencies are of the order $\omega_p \sim 10^{12}$–$10^{14}\ \text{s}^{-1}$. In this regime, the absorption coefficient typically falls within $\alpha_{\text{IB}} \sim 10^2$–$10^5\ \text{m}^{-1}$, indicating substantial attenuation of the laser field over sub-millimetre propagation distances, [13], [14], [15]. The ω^2 term in the denominator of Eq. (3) introduces a direct dependence of the absorption efficiency on the laser wavelength. As a result, longer wavelengths lead to stronger collisional heating of electrons and favor the development of avalanche ionization (AI), whereas at shorter wavelengths the energy gain of free electrons is reduced and plasma formation remains more strongly influenced by the initial multiphoton seeding. Therefore, the interplay between MPI and avalanche growth is governed by the wavelength-dependent balance between electron generation and energy absorption, which forms the basis of the analysis presented in the following section.

As already mentioned, the separation of timescales provides the physical basis for introducing a two-temperature description of the plasma. To capture this nonequilibrium behaviour, separate energy balance equations are introduced for the electron and heavy-particle subsystems. The electron energy equation accounts for laser absorption, energy exchange with heavy particles, ionization losses, and thermal transport, and can be written as follows, [13], [15]:

$$\frac{\partial}{\partial t}\left(\frac{3}{2}n_e k_B T_e\right) = \alpha_{\mathrm{IB}} I - \frac{3}{2}n_e k_B \nu_{eh}(T_e - T_h) - E_I(S_{\mathrm{MPI}}+S_{\mathrm{av}}) + \frac{\partial}{\partial x}\left(\kappa_e \frac{\partial T_e}{\partial x}\right). \quad (5)$$

Here T_e and T_h denote the electron and heavy-particle temperatures, respectively. The first term on the right-hand side represents energy gain due to IB absorption, while the second term describes collisional energy transfer toward equilibrium. The ionization energy loss term accounts for both MPI and AI processes, assuming that each generated electron requires an average energy E_I. The third term accounts for the energy required for ionization, and the last term represents electron thermal conduction. For the considered plasma conditions, the electron thermal conductivity is typically in the range $\kappa_e \sim 0.1\text{–}10\ \mathrm{W\,m^{-1}\,K^{-1}}$, depending on the local electron temperature and collision frequency. In the present simulations, the electron thermal conductivity is treated as weakly temperature-dependent and evaluated using representative local plasma parameters. Further, the heavy-particle temperature, T_h, evolves according to a corresponding balance equation:

$$\frac{\partial}{\partial t}\left(\rho c_p T_h\right) = \frac{3}{2}n_e k_B \nu_{eh}(T_e - T_h) + \frac{\partial}{\partial x}\left(\kappa_h \frac{\partial T_h}{\partial x}\right), \quad (6)$$

where ρ is the mass density and c_p is the specific heat capacity of the gas. Under ambient conditions, $\rho \approx 1.2\ \mathrm{kg\,m^{-3}}$ and $c_p \approx 1005\ \mathrm{J\,kg^{-1}\,K^{-1}}$. The thermal conductivity of the heavy particles is taken as $\kappa_h \sim 0.02\text{–}0.05\ \mathrm{W\,m^{-1}\,K^{-1}}$, consistent with air at near-atmospheric conditions. The coupling term is proportional to ν_{eh} governs the transfer of energy from electrons to heavy particles; however, because this process occurs at a finite rate, thermal equilibration is delayed. Consequently, during the laser pulse the electron temperature can rise to significantly higher values, whereas the heavy-particle subsystem heats more gradually. This nonequilibrium thermal behavior plays a crucial role in the efficiency of AI and the subsequent plasma evolution. Since the electron temperature directly affects the collision frequency, it also controls the efficiency of IB absorption, thereby establishing a feedback mechanism that promotes cascade ionization growth. At longer wavelengths, stronger collisional heating results in higher electron temperatures and enhanced avalanche development, while at shorter wavelengths, weaker energy coupling suppresses the amplification of the initially generated electron population.

The combined treatment of electron density evolution, wavelength-dependent absorption, and two-temperature energy exchange therefore provides a self-consistent framework for analyzing the LIB dynamics discussed in the following section.

3 Results and Disscusion

In Figure 1 we present the axial distribution of the peak electron density $n_e(x)$ for two wavelengths, $\lambda = 355\ nm$ and $\lambda = 532\ nm$.

The peak electron density is defined as the maximum value of $n_e(x,t)$ reached during the laser pulse at each axial position, and it shows how strongly the gas is ionized locally. The coordinate x is taken along the direction of laser propagation, with $x = 0$ corresponding to the focal position where the laser intensity is highest. The shown interval ± 0.5 mm, covers the region around the focus where the laser beam is sufficiently intense to produce ionization. Outside this region, the intensity rapidly decreases due to beam spreading, and the electron density falls to its background level. In this way, the profiles in Figure 1 show how the electron population is built along the propagation axis and how the balance between MPI and avalanche growth determines both the magnitude and the extent of the plasma channel.

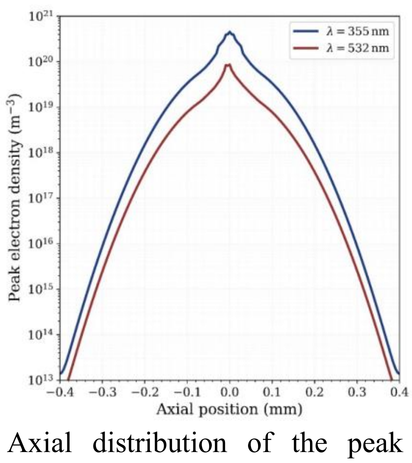

Fig. 1: Axial distribution of the peak electron density $n_e(x)$ for laser wavelengths of $\lambda = 355\ nm$ and $\lambda = 532\ nm$.
Source: created by the authors.

The axial profiles shown in Figure 1 reveal a pronounced wavelength dependence of both the magnitude and spatial development of the electron density, reflecting the underlying balance between seeding and energy-driven amplification mechanisms. As a direct consequence of the more efficient IB absorption at the longer wavelengths at 532 nm, the electron density rises by several orders of magnitude relative to the 355 nm case, resulting in a broader and more smoothly distributed plasma region around the focal area. The lower laser frequency at 532 nm enables a more efficient transfer of energy from the laser field to the electron population. Consequently, even a small concentration of seed electrons can gain enough energy to initiate EII, leading to an AI process that rapidly increases the electron density over a wider axial region because the increased electron temperature enhances the collision frequency and sustains efficient energy absorption while the laser intensity remains sufficiently high. At 352 nm, the higher laser frequency reduces the efficiency of collisional (inverse Bremsstrahlung) absorption, and electrons gain energy less effectively despite stronger MPI seeding. Although MPI provides an initial seed electron population, its energy is insufficient to sustain significant EII, and the AI is largely suppressed. As a result, the electron density remains low and more tightly confined around the focal region.

In Figure 2 the temporal evolution of the electron temperature T_e and the heavy-particle temperature T_h at the focal position ($x = 0$) for the two wavelengths is considered.

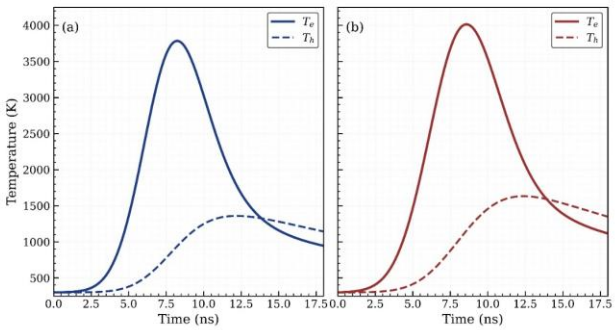

Fig. 2: Temporal evolution of the electron temperature T_e and the heavy-particle temperature T_h at the focal position ($x = 0$) for two laser wavelengths: (a) 355 nm and (b) 532 nm.
Source: created by the authors.

As shown by the curve shapes, a characteristic sequence emerges: rapid electron heating, followed by delayed gas heating and a subsequent relaxation of the system. The 532 nm case exhibits a stronger overall thermal response, as this wavelength more efficiently supports electron heating and, in turn, enhances energy transfer to the surrounding gas. For both wavelengths, the electron temperature T_e rises rapidly and reaches its maximum, with $T_{e,\max} = 3783.58\,\text{K}$ near $t \approx 8.23$ ns (Figure 2(a)) and $T_{e,\max} = 4013.22\,\text{K}$ near $t \approx 8.58$ ns (Figure 2(b)). The heavy-particle temperature T_h, by contrast, responds more slowly and attains its maximum, T_{h_max} only several nanoseconds later, at $t = 12.18$ ns for 355 nm, $T_{h\_max} = 1359.56\,\text{K}$ (Figure 2(a)) and $t = 12.38$ ns for 532 nm, $T_{h\_max} = 1632.64\,\text{K}$ (Figure 2(b)). The delay between the maxima of T_e and T_h response is characteristic of a two-temperature plasma system: electrons absorb the laser energy first, while the gas temperature increases only after successive collisions transfer this energy to neutral and heavy particles. This behavior is fully consistent with the expected dynamics of weakly ionized plasmas, [16]. Both T_e and T_h are higher at 532 nm, and that is consistent with the more efficient IB heating at longer wavelengths, [12]. The difference between the two temperatures remains large in both cases, with $\Delta T_{\max} = 2424.02\,\text{K}$ for 355 nm (Figure 2(a)) and $\Delta T_{\max} = 2380.57\,\text{K}$ for 532 nm (Figure 2(b)), showing that the plasma does not approach thermal equilibrium during the main stage of energy deposition.

To further characterize the breakdown dynamics beyond the spatial snapshots discussed previously, we examine in Figure 3 the temporal evolution of two key quantities derived from the model: the on-axis electron density $n_e(0, t)$ (Figure 3(a)) and the effective width of the plasma channel $w_{\text{eff}}(t)$ (Figure 3(b)). The quantity $n_e(0, t)$ is the solution of the continuity equation, Eq. (1), evaluated at the focal point $x = 0$, where the laser intensity reaches its maximum, and the interplay between generation and loss processes is most pronounced. In Figure 3(b), the effective channel width is introduced $w_{\text{eff}}(t)$ as a characteristic measure of the spatial extent of the plasma along the propagation axis. The introduction of $w_{\text{eff}}(t)$ makes it possible to monitor not only the local plasma growth at the focal region, but also its expansion along the propagation axis. This provides deeper insight into the formation and temporal evolution of the plasma channel under different laser wavelength conditions. Such understanding is particularly important for practical applications involving laser–matter interaction, including laser micromachining, filamentation control, plasma-based light guiding, and optimization of laser-induced material processing.

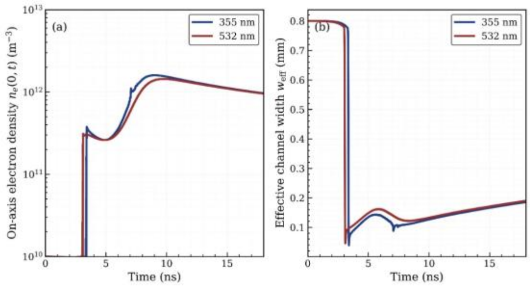

Fig. 3: Temporal evolution of: (a) the on-axis electron density $n_e(0,t)$ and (b) the effective plasma channel width $w_{\mathrm{eff}}(t)$ for laser wavelengths of 355 nm and 532 nm.
Source: created by the authors.

The temporal evolution of the on-axis electron density in Figure 3(a) illustrates the nonlinear interplay between ionization, avalanche amplification, and loss processes. Initially, the electron density remains close to its background value, since ionization is insufficient to overcome recombination and diffusion. As the laser pulse approaches its peak, avalanche ionization becomes dominant, causing a rapid increase in electron density followed by saturation and a gradual decay. This behaviour is much more pronounced at 532 nm, where the sharper rise, higher saturation level, and slower decay indicate a strongly developed avalanche regime. In contrast, the 355 nm case exhibits a smoother increase and faster decay, characteristic of a weaker, seeding-controlled regime.

The evolution of the effective channel width in Figure 3(b) reflects the coupling between ionization and transport. Before the breakdown, w_{eff} remains nearly constant, corresponding to the laser beam size. During rapid avalanche growth, a sharp reduction of w_{eff} occurs due to the localization of the plasma near the focal region, particularly at 532 nm. This is followed by re-expansion of the plasma channel driven by diffusion and sustained ionization. The recovery is stronger at 532 nm, indicating enhanced transport and secondary ionization processes. Overall, the results show that longer wavelengths produce denser and more spatially extended plasma channels, while shorter wavelengths lead to weaker and more localized plasma formation.

4 Conclusion

We use a two-temperature model to numerically analyze the wavelength dependence of LIB in ambient air. The obtained results show that LIB is driven by the complex nonlinear interaction between the initial creation of free electrons and their later energy uptake from the laser field. For the 355 nm wavelength, MPI effectively generates the initial seed electrons, but the acquired electron energy is insufficient to maintain efficient EII. Therefore, the increase in electron density remains limited, and the resulting plasma stays relatively confined in space. In contrast, at 532 nm, the stronger collisional absorption produces more efficient electron heating, which significantly enhances EII. This establishes a positive feedback loop between electron multiplication and laser energy deposition, leading to rapid plasma amplification and the development of a dense plasma channel. The calculated temporal behaviour of electron and heavy-particle temperatures also demonstrates that the breakdown process evolves under strongly nonequilibrium conditions. Electrons respond almost instantaneously to the laser field, while the heavy-particle subsystem heats more slowly, producing a long-lasting temperature imbalance that affects the overall plasma energy dynamics. Furthermore, the simultaneous evolution of electron density and plasma radius indicates that the breakdown exhibits threshold-like behaviour. Once the ionization level exceeds a critical value, the plasma becomes highly localized around the focal region and subsequently expands because of diffusion and ongoing energy transfer processes. These findings collectively suggest that the laser wavelength governs not only the prevailing ionization mechanism but also the effectiveness of energy coupling and the resulting temporal and spatial evolution of the plasma structure.

Acknowledgement:
Authors would like to acknowledge the support received from the Science Fund of the Republic of Serbia, #GRANT 6821, Atoms and (bio) molecules-dynamics and collisional processes on short time scale - ATMOLCOL. Our appreciation also goes to the Serbian Ministry of Education, Science and Technological Development (Agreement No. 451-03-34/2026-03/200122).

References:
[1] Smith D. C., Laser radiation-induced air breakdown and plasma shielding, *Optical Engineering*, Vol.20, No.6, 1981, pp. 962-969. https://doi.org/10.1117/12.7972843.
[2] Niu C., Hu Z., Cheng X., Gong A., Wang K., Zhang D., Li S., Guo, L., Individual micron-sized aerosol qualitative analysis–combined

Raman spectroscopy and laser-induced breakdown spectroscopy by optical trapping in air, *Analytical Chemistry*, Vol.95, No.5, 2023, pp. 2874-2883.
https://doi.org/10.1021/acs.analchem.2c04411

[3] Sacchi C.A., Laser-induced electric breakdown in water, *Journal of the Optical Society of America B,* Vol.8, No.2, 1991, pp. 337-345,
https://doi.org/10.1364/JOSAB.8.000337.

[4] Förster, D.J., Jäggi, B., Michalowski, A., Neuenschwander, B., Review on experimental and theoretical investigations of ultra-short pulsed laser ablation of metals with burst pulses. *Materials*, Vol.14, No.12, 2021, p. 3331, https://doi.org/10.3390/ma14123331.

[5] Mühlberger F., Hafner K., Kaesdorf S., Ferge T., Zimmermann R., Comprehensive on-line characterization of complex gas mixtures by quasi-simultaneous resonance-enhanced multiphoton ionization, vacuum-UV single-photon ionization, and electron impact ionization in a time-of-flight mass spectrometer: setup and instrument characterization, *Analytical Chemistry*, Vol.76, No.22, 2004, pp.6753-6764.
https://doi.org/10.1021/ac049535r.

[6] Gamaly E.G., Rode A.V., Transient optical properties of dielectrics and semiconductors excited by an ultrashort laser pulse, *Journal of the Optical Society of America B*, Vol.31, No.11, 2014, pp: C36-C43.
https://doi.org/10.1364/JOSAB.31.000C36.

[7] Tate J.T., Smith P.T., The efficiencies of ionization and ionization potentials of various gases under electron impact, *Physical Review*, Vol.39, No.2, 1932, p:27. doi: 10.1103/PhysRev.39.270.

[8] Tien A.C., Backus S., Kapteyn H., Murnane M., Mourou G., Short-pulse laser damage in transparent materials as a function of pulse duration, *Physical Review Letters*, Vol.82, No. 19, 1999, pp: 3883-3886.
https://doi.org/10.1103/PhysRevLett.82.3883.

[9] Wu Y., Xiang X., Yu J., Yuan X., Shen H., Zheng W., Zu X., Research progress on nanosecond laser irradiation damage of optical films, *Nuclear Analysis*, Vol.1, No.4, 2022, Article: 100045.
doi: 10.1016/j.nucana.2022.100045.

[10] Hossain M.F., Sohan M.S.R., Hasan M., Miah M.M., Sajib S.A., Karmakar S., Khalid-bin-Ferdaus K.M., Kabir A.H., Rashid M.M., Talukder M.R., Reza M.A., Enhancement of seed germination rate and growth of maize (*Zea mays* L.) through LPDBD Ar/Air plasma, *Journal of Soil Science and Plant Nutrition*, Vol.22, No.2, 2022, pp. 1778–1791. doi: 10.1007/s42729-022-00771-6.

[11] Raĭzer Y.P., Breakdown and heating of gases under the influence of a laser beam, *Soviet Physics Uspekhi*, Vol.8, No.5, 1966, pp. 650–673.
doi: 10.1070/PU1966v008n05ABEH003027.

[12] Rethfeld B., Ivanov D.S., Garcia M.E., Anisimov S.I., Modelling ultrafast laser ablation, *Journal of Physics D: Applied Physics*, Vol.50, No.19, 2017, Article: 193001. doi: 10.1088/1361-6463/50/19/193001.

[13] Raizer Y.P., Allen J.E., *Gas Discharge Physics*, Berlin, Springer, 1997. ISBN: 3-540-19462-2 Springer-Verlag Berlin Heidelberg New York.

[14] Wang Z., Afgan M.S., Gu W., Song Y., Wang Y., Hou Z., Song W., Li Z., Recent advances in laser-induced breakdown spectroscopy quantification: From fundamental understanding to data processing, *TrAC Trends in Analytical Chemistry*, Vol. 143, 2021, Article: 116385.
https://doi.org/10.1016/j.trac.2021.116385.

[15] Ikeda Y., Soriano J.K., Microwave-enhanced laser-induced air plasma at atmospheric pressure, *Optics Express*, Vol. 30, No. 19, 2022, pp. 33756–33766. doi: 10.1364/OE.470072.

[16] Semenov I.L., Moment fluid equations for ions in weakly ionized plasma, *Physical Review E*, Vol.95, No.4, 2017, Article: 043208.
https://doi.org/10.1103/PhysRevE.95.043208.

Contribution of Individual Authors to the Creation of a Scientific Article (Ghostwriting Policy)

The authors equally contributed in the present research, at all stages from the formulation of the problem to the final findings and solution.

Sources of Funding for Research Presented in a Scientific Article or Scientific Article Itself

The research presented in this scientific article was funded by the Science Fund of the Republic of Serbia, Grant No. 6821, *Atoms and (Bio)Molecules: Dynamics and Collisional Processes on Short Time Scales (ATMOLCOL)*. The authors also acknowledge support from the Ministry of Science, Technological Development and Innovation of the Republic of Serbia under Agreement No. 451-03-34/2026-03/200122.

Conflict of Interest

The authors have no conflicts of interest to declare that are relevant to the content of this article.